

High-performance Bragg gratings in chalcogenide rib waveguides written with a modified Sagnac interferometer

Mehrdad Shokooh-Saremi

Centre for Ultrahigh-Bandwidth Devices for Optical Systems, School of Physics, University of Sydney, New South Wales 2006, Australia, and Faculty of Electrical Engineering and Robotics, Shahrood University of Technology, Iran

Vahid G. Ta'eed, Neil J. Baker, Ian C. M. Littler, David J. Moss, and Benjamin J. Eggleton

Centre for Ultrahigh-Bandwidth Devices for Optical Systems, School of Physics, University of Sydney, New South Wales 2006, Australia

Yinlan Ruan and Barry Luther-Davies

Centre for Ultrahigh-Bandwidth Devices for Optical Systems, Laser Physics Centre, The Australian National University, Canberra, Australian Capital Territory 0200, Australia

Received July 22, 2005; revised February 15, 2006; accepted February 15, 2006; posted March 16, 2006 (Doc. ID 63612)

We demonstrate the highest-quality Bragg gratings reported to date in chalcogenide glass rib waveguides, both in strength and apodization. A modified Sagnac interferometer is employed to write gratings in As_2S_3 -based rib waveguides, achieving an induced refractive index modulation of the order of 10^{-2} and a grating transmission rejection of more than 30 dB. We obtain good agreement between experimental and theoretical results based on a transfer-matrix formulation for multilayer optical structures. In addition, we report fabrication of phase-shifted Bragg gratings, as well as an investigation of the role of birefringence, higher-order modes, and aging. Finally, grating growth dynamics are investigated by *in situ* monitoring during writing. © 2006 Optical Society of America

OCIS codes: 350.2770, 190.4390, 130.3120.

1. INTRODUCTION

Chalcogenide glasses (ChGs) have attracted significant interest in the past several years¹ as a promising platform for both integrated and fiber-based all-optical devices for future ultrahigh bit-rate optical communication systems. Collectively, this class of glasses exhibits many attractive features required for nonlinear all-optical devices, such as high nonlinearity (with third-order Kerr optical nonlinearities reported up to 1000 times silica),^{1,2} low two-photon absorption in the 1.55 μm optical telecommunications band, photosensitivity to visible light, and the ability to tailor linear and nonlinear optical properties by adjusting stoichiometry. The ability to write Bragg gratings in ChG waveguides via their photosensitivity³ offers a powerful addition to the large intrinsic nonlinearity and is highly promising for nonlinear all-optical devices such as optical regenerators⁴⁻⁶ and switches based on gap solitons.^{7,8} For these all-optical applications, the quality of the grating filter (high extinction ratio, suitably wide spectral bandwidth, high sidelobe level suppression, and good apodization) is a key factor in overall device performance.

In this paper, we present high-performance Bragg gratings in As_2S_3 -based rib waveguides written with a modified Sagnac interferometer. We achieve 7 nm wide gratings with a corresponding refractive index modulation of

10^{-2} and more than 30 dB in transmission rejection. We also achieve good grating apodization (using the writing laser coherence length) resulting in sidelobe suppression better than 25 dB. Furthermore, we obtain good agreement between experimental and theoretical results based on a 2×2 transfer-matrix formulation for multilayer structures.⁹ We also report the first demonstration of phase-shifted Bragg gratings in chalcogenide-based rib waveguides, fabricated using a photomask, and obtain a central transmission bandwidth of less than 100 pm. The influence of waveguide birefringence, higher-order modes (HOMs), and aging on the grating spectra are also investigated. Finally, grating growth dynamics are studied during writing by an *in situ* monitoring system, and spectra are compared with the modeling results.

ChGs, which contain chalcogen elements (S, Se, and Te) and other elements such as As, Ge, Sb, and Ga, are low-phonon-energy materials, generally transparent from the visible to the infrared. They typically have high optical nonlinearities with a nonlinear Kerr refractive index (n_2) up to 1000 times that of silica.² In addition, these large nonlinearities can be achieved while still maintaining low two-photon absorption. Figures of merit ($n_2/\beta\lambda$, in which β is the two-photon absorption coefficient) higher than 12 have been achieved in As_2S_3 in the telecommunication wavelength band.¹⁰ In this work, we focus on As_2S_3 ChG

that has recently formed the basis of low-loss rib waveguides fabricated by the ultrafast pulsed laser deposition technique.¹¹ Among the various types of ChGs, As_2S_3 displays a relatively high n_2 value and is one of the most well studied. As_2S_3 has a bandgap energy of 2.4 eV ($\lambda_{\text{gap}}=517$ nm) and linear (n_0) and nonlinear (n_2) refractive indices of 2.38 and 3.8×10^{-14} cm²/W, respectively.^{12–14} In addition, As_2S_3 is well known to be photosensitive to visible light using Ar^+ (514 nm) and He–Ne (632.8 nm) lasers.^{15,16} This has been used to fabricate low-loss (<0.3 dB/cm) channel waveguides and waveguide Bragg gratings, fiber amplifiers, and lasers.¹²

The central feature of this paper is the demonstration of high-quality Bragg gratings adequate for demanding high-bit-rate all-optical device applications as well as the first complex grating structures containing phase shifts. The structure of the paper is as follows. First, the waveguide structure is described, followed by a discussion of the grating writing setup. Next, grating writing results are presented along with numerical modeling. The effects of waveguide birefringence, HOMs, and aging are then discussed. Finally, grating growth dynamics, measured with an embedded *in situ* monitoring system, are presented.

2. WAVEGUIDE STRUCTURE AND WRITING SETUP

A. Waveguide Structure

The As_2S_3 -based rib waveguides are fabricated by deposition of an As_2S_3 layer onto a thermally oxidized silicon wafer utilizing the ultrafast pulsed laser deposition technique with a frequency-doubled, mode-locked Nd:YAG laser.¹¹ The 2.4 μm thick SiO_2 layer provides a lower cladding layer with a refractive index ($n_{\text{silica}}=1.44$) much less than As_2S_3 . Ultrafast pulsed laser deposition produces atomically smooth, dense thin films, which usually do not require annealing before subsequent fabrication processes. We use a standard photolithographic technique with an aluminum mask followed by helicon plasma dry etching with a CF_4/O_2 gas mixture as the etchant (etch rate=250 nm/min) to form a rib waveguide (rib height $H=2.0$ – 5.0 μm , slab height $h=1.0$ – 1.7 μm). After etching, a high-quality polysiloxane layer ($n=1.53$) is deposited (thickness > 10 μm) to act as a protective overlaid layer.¹¹ Waveguide widths vary from 3 to 5 μm . Figure 1 shows a schematic view of a typical waveguide, as well as an optical micrograph of a waveguide facet. Propagation losses of the waveguides are dependent on the effective area and polarization. Both cutback¹⁷ and Fabry–Perot waveguide cavity fringe analysis¹⁸ were used to measure propagation losses, which were ~ 0.25 dB/cm at 1.55 μm for the wider waveguides. Although the deep etch depth of the waveguides (>45%) resulted in tight light confinement in the rib region, making them attractive for nonlinear optical experiments such as self-phase modulation,¹¹ the relatively large effective area of the wider waveguides resulted in the support of higher-order TE and TM modes.^{19,20}

B. Grating Writing Setup and Characterization

Figure 2 shows the holographic grating writing setup, based on a modified Sagnac interferometer, used to write the Bragg gratings in the As_2S_3 rib waveguides.²¹ To date, in reports of holographically written Bragg gratings in ChG-based fibers and waveguides, Mach–Zehnder interferometers have been employed,^{15,16,22–24} which are par-

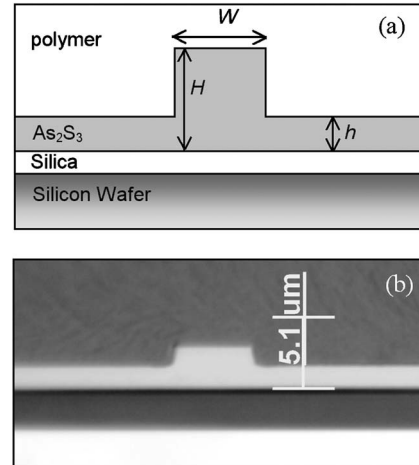


Fig. 1. (a) Schematic cross section of an As_2S_3 -based rib waveguide and (b) an optical micrograph of a waveguide.

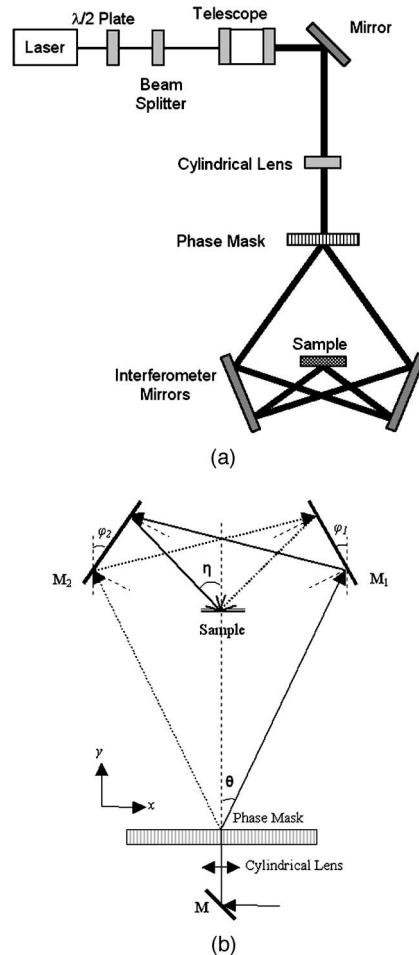


Fig. 2. (a) Schematic of the grating writing setup based on the modified Sagnac interferometer and (b) the interferometer structure used to derive the equations.

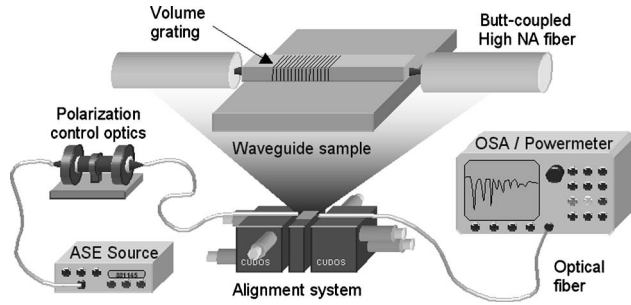


Fig. 3. Waveguide and grating characterization setup. ASE, amplified spontaneous emission, OSA, optical spectrum analyzer.

ticularly sensitive to environmental disturbances (mechanical vibrations, thermal gradients, and air currents). This sensitivity affects the stability of the interference pattern over time and hence the quality of the Bragg grating—especially during long write times. In contrast, a Sagnac interferometer provides excellent stability over time. Using a vertical vacuum sample holder enabled us to implement the writing system horizontally. We used the modified Sagnac interferometer in combination with a cw, frequency-doubled, diode-pumped Nd:YAG laser ($\lambda_w = 532$ nm) with a maximum available power at the sample of 50 mW. The laser had a short coherence length (~ 3 mm) that we used to apodize the edges of the grating via the length-dependent visibility of the interference pattern,²⁵ which is discussed in detail in Section 3. The polarized laser beam was telescopically expanded, cylindrically focused, and split using a phase mask with rectangular grooves ($\Lambda_m = 1063.3$ nm). The angle between each ± 1 diffracted order and the normal axis to the phase mask surface (θ), shown in Fig. 2(b), is fixed at $\theta = \sin^{-1}(\lambda_w/\Lambda_m)$.

The ± 1 diffracted orders of the phase mask are reflected from a pair of mirrors and interfere at the sample surface (TE polarized). The spot size at the writing plane was measured with a laser beam analyzer to be 6.0 mm (width) \times 0.6 mm (height). The half-angle between the two interfering beams at the surface of the sample (η) is given by $\eta = \pi - 2\varphi_1 - 2\varphi_2 - \theta$, where φ_1 and φ_2 are the angles of the two interferometer mirrors. The Bragg wavelength (λ_B) of the written grating is

$$\lambda_B = \frac{n_{\text{eff}}\lambda_w}{\sin(\pi - 4\varphi - \theta)} = \frac{n_{\text{eff}}\lambda_w}{\sin(\eta)}, \quad (1)$$

where n_{eff} is the effective refractive index of the waveguide propagating mode and we assume that $\varphi_1 = \varphi_2 = \varphi$. Clearly then, n_{eff} and φ (or η) are the two main parameters that affect the Bragg wavelength. The sensitivity of the Bragg wavelength to n_{eff} and η is

$$\Delta\lambda_B = \frac{\lambda_w}{\sin(\eta)} \Delta n_{\text{eff}}, \quad (2)$$

$$\frac{\Delta\lambda_B}{\lambda_B} = -\cot(\eta) \Delta\eta. \quad (3)$$

For example, $\Delta n_{\text{eff}} = 0.02$ or $\Delta\eta = 1^\circ$ results in a Bragg wavelength deviation of around 20 nm. Thus the Bragg

wavelength can be arbitrarily set by adjusting the sample holder position and tuning the mirror angles.

Figure 3 shows the schematic view of the characterization setup. The transmission spectra of the gratings were characterized using an unpolarized erbium-doped fiber amplifier, an amplified spontaneous emission (ASE) source (C band: 1520–1580 nm), and an optical spectrum analyzer (OSA) with 60 pm resolution. A fiber-coupled, bulk optics polarization controller stage was placed between the light source and the sample and adjusted to obtain the maximum polarization extinction ratio for the two orthogonal polarization states (TE and TM). The source was then butt coupled into the waveguide via a high numerical aperture (NA) fiber. A second high-NA fiber coupled the transmitted output either to an optical powermeter for alignment optimization or to the OSA to measure the transmission spectra. The output polarization state of the waveguide was verified using a bulk optics polarizer.

3. EXPERIMENTAL RESULTS

Figure 4 shows the transmission spectrum of a strong, high-quality Bragg grating for TE-polarized light, written in a 4 μm wide ($H = 2.39$ μm , $h = 1.39$ μm), 5 cm long As_2S_3 rib waveguide using the modified Sagnac setup. The sample was exposed to a total writing power of 6.0 mW for 60 s. The sharp spectral features, wide spectral bandwidth ($\Delta\lambda \sim 5$ nm corresponding to $\Delta n_{\text{ac}} \sim 7.7 \times 10^{-3}$), and deep transmission rejection of -33 dB are indications of the stability of the Sagnac setup. Note that the minimum of the transmission dip is less than -33 dB but cannot be resolved by our measurement system. The shallow transmission dip near 1544.5 nm is due to a HOM, which this waveguide supports, and is discussed in Subsection 5.C.

The strong suppression of sidelobes around the main resonance in Fig. 4 is particularly noteworthy. Appearance of such sidelobes is a result of a Fabry–Perot-like cavity effect caused by abrupt changes in the grating structure, such as would occur at the beginning and end of a uniform Bragg grating. In practical applications, these spectral sidelobes are suppressed by apodization: a process of slowly varying the grating structure along its axis, resulting in a nonuniform grating profile.²⁶ The near

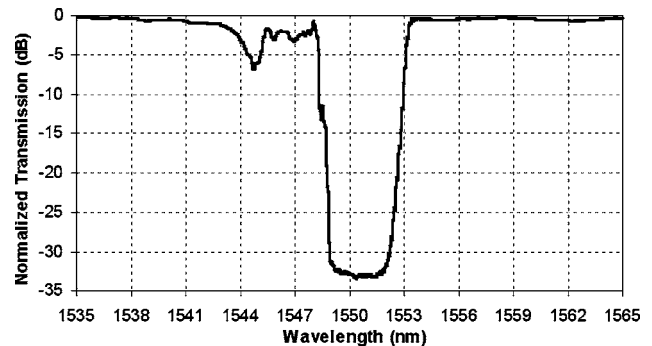


Fig. 4. Normalized transmission spectrum of a strong, well-apodized grating for TE polarization. This grating has been written in a 4 μm wide and 5 cm long waveguide ($H = 2.39$ μm , $h = 1.39$ μm).

absence of sidelobes in our transmission spectra indicates that the grating profile has been properly apodized. This was achieved by utilizing the short coherence length of the laser (~ 3 mm)²⁵ to produce high-visibility interference fringes that gradually diminish over a length scale related to the coherence length and hence the suppression of the sidelobes. In addition, the interfering beams at the surface of the sample have a Gaussian profile 6.0 mm in length. Since the coherence length is shorter than the exposed length, the average refractive index in the grating region is relatively flat, resulting in a raised Gaussian-apodized structure. This ensures that the Bragg wavelength remains constant over the grating structure. It should be mentioned that Gaussian-interfering beams with long coherence length would not result in a uniform average refractive index. The Bragg wavelength in such a structure would vary as a function of position, causing Fabry–Perot-like fringes to appear on the short wavelength side of the transmission dip.²⁶

4. MODELING

To model the gratings we use a thin-film 2×2 transfer-matrix method (T matrix),⁹ which is more rigorous than other techniques such as a matrix formulation of the coupled-mode equations.²⁷

Figure 5 shows a general multilayer dielectric structure. In this figure, $\{(n_i, d_i), i=1, 2, \dots, N\}$ are the refractive indices and thicknesses of the layers, respectively, and n_0 and n_s are the refractive indices of the incident and substrate media. A_0, B_0, A_{N+1} , and B_{N+1} are the incident, reflected, transmitted, and incident from the substrate (equal to zero) electric field amplitudes, respectively. The relation between the field amplitudes in the incident and substrate media is

$$\begin{bmatrix} A_0 \\ B_0 \end{bmatrix} = \mathbf{M} \begin{bmatrix} A_{N+1} \\ B_{N+1} \end{bmatrix}, \quad (4)$$

where \mathbf{M} is a 2×2 matrix with the following form:

$$\mathbf{M} = \begin{bmatrix} M_{11} & M_{12} \\ M_{21} & M_{22} \end{bmatrix} = \mathbf{D}_0^{-1} \left(\prod_{i=1}^N \mathbf{Q}_i \right) \mathbf{D}_s, \quad (5)$$

where \mathbf{D}_0 and \mathbf{D}_s are the dynamic matrices of the incident medium and substrate, respectively, and \mathbf{Q}_i is the characteristic matrix of the i th layer. At an angle of incidence equal to zero, the above matrices are

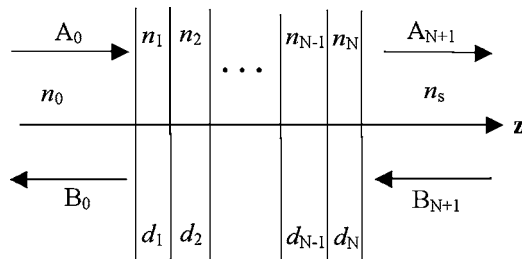


Fig. 5. General schematic view of a multilayer dielectric structure. The n 's and d 's are the layer refractive indices and thicknesses, respectively.

$$\mathbf{D}_0 = \begin{bmatrix} 1 & 1 \\ n_0 & -n_0 \end{bmatrix}, \quad \mathbf{D}_s = \begin{bmatrix} 1 & 1 \\ n_s & -n_s \end{bmatrix}, \quad (6)$$

$$\mathbf{Q}_i = \begin{bmatrix} \cos \varphi_i & \frac{j}{n_i} \sin \varphi_i \\ j n_i \sin \varphi_i & \cos \varphi_i \end{bmatrix}. \quad (7)$$

In Eq. (7), $\varphi_i = (2\pi/\lambda)n_i d_i$ is the effective optical thickness of the i th layer. The reflectance (R) and transmittance (T) from the layered structure are related to the matrix \mathbf{M} elements

$$R = \left| \frac{M_{21}}{M_{11}} \right|^2, \quad T = \frac{n_s}{n_0} \left| \frac{1}{M_{11}} \right|^2. \quad (8)$$

5. GRATING PROPERTIES

To model the gratings, the complete grating structure is discretized. We found that a layer thickness equal to a quarter of the grating period is sufficient to efficiently follow the sinusoidal refractive index variation. Also, as mentioned above, to eliminate the spectral sidelobes, a raised apodization profile is required, which is the motivation behind our use of a short-coherence-length laser.²⁵ Under these conditions, the effective length of the grating (L_g , approximately equal to the coherence length of the writing laser) is shorter than the length of the total exposed area (L_t). The refractive index profile of a typical raised Gaussian-apodized grating is

$$n(z) = n_0 + \Delta n_{dc} \exp \left[-\frac{z^2}{2(L_t/6)^2} \right] \times \left\{ 1 + \nu \exp \left[-\frac{z^2}{2(L_g/4)^2} \right] \cos \left(\frac{2\pi}{\Lambda} z \right) \right\}, \quad (9)$$

where n_0 is the linear refractive index that is close to the effective refractive index of the fundamental mode as calculated by the beam propagation method,²⁸ Δn_{dc} is the dc refractive index change, ν is the visibility, and Λ is the period. The index modulation amplitude (Δn_{ac}) is then

$$\Delta n_{ac} = \Delta n_{dc} \nu \exp \left(-\frac{z^2}{2(L_g/4)^2} \right) \exp \left[-\frac{z^2}{2(L_t/6)^2} \right]. \quad (10)$$

A. Strong, Well-Apodized Bragg Gratings

Figure 6 shows the experimental normalized transmission spectrum (TE polarization) of a strong grating fabricated with 10.0 mW writing power and 60 s exposure in a 5.3 cm long As_2S_3 rib waveguide ($W=4$ μm , $H=2.37$ μm , $h=1.25$ μm). Shown concurrently are the theoretical results modeled using the 2×2 T -matrix method together with the grating profile in Eq. (9). The grating parameters are $n_0=2.37$, $\Delta n_{dc}=0.0096$, $\nu=1$, $L_t=7$ mm, $L_g=3$ mm, and $\lambda_B=1552.5$ nm. As can be seen, this is a well-apodized grating with highly suppressed sidelobes on the short wavelength side of the spectrum, achieved through the short coherence length of the writing laser.

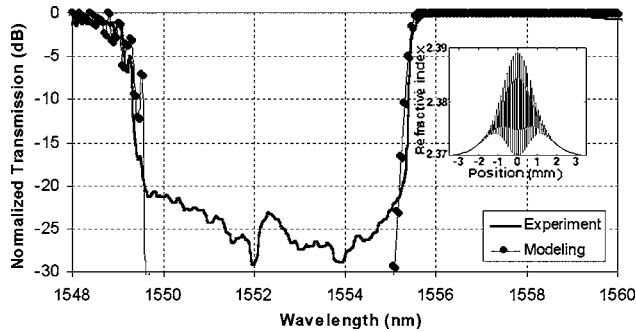


Fig. 6. Experimental and theoretical normalized transmission spectra of a strong grating fabricated in a 5.3 cm long As_2S_3 rib waveguide ($W=4 \mu\text{m}$, $H=2.37 \mu\text{m}$, $h=1.25 \mu\text{m}$). The specifications of the waveguide and grating are $n_0=2.37$, $\Delta n_{\text{dc}}=0.0096$, $\nu=1$, $L_f=7 \mu\text{m}$, $L_g=3 \text{mm}$, and $\lambda_B=1552.5 \text{nm}$. Inset: the grating profile used for modeling.

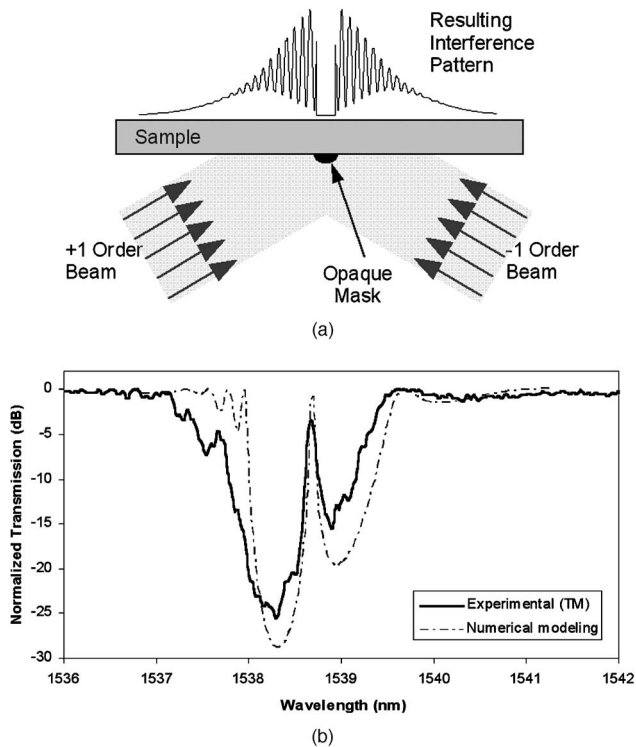


Fig. 7. (a) Mechanism of introduction of a defect by an opaque mask into the grating structure to obtain a phase-shifted grating and (b) experimental transmission spectrum (solid curve) of the resulting phase-shifted grating (TM polarization) versus the spectrum obtained from modeling (dashed-dotted curve).

B. Phase-Shifted Bragg Gratings

Because of the strongly enhanced fields they generate, phase-shifted Bragg gratings, as high-finesse notch filters, have great potential for application in nonlinear devices, allowing for greatly reduced switching thresholds.²⁹ Such gratings are fabricated by introducing a phase shift across the grating. The main techniques employed for fabrication of phase-shifted gratings are (1) incorporation of the phase shift in the fabrication mask,³⁰ (2) postexposure of the grating structure,³¹ (3) postprocessing using localized heat treatment,^{32,33} and (4) utilizing an opaque mask to block the interfering beams in part of the grating structure. All of the mentioned techniques effectively result in

two gratings that act as a Fabry–Perot cavity. Method 1 is not suitable for the current interferometric setup, method 3, in which heat treatment is used, is not compatible with our waveguides because of the polymer overcoating. Methods 2 and 4 are both compatible with our waveguides and method 4 is used here. The resonance wavelength depends on the magnitude of the phase shift and is related to the width of the cavity. The width also affects the free spectral range of the Fabry–Perot resonator. The location of the cavity within the grating structure affects the relative reflectivity of the two cavity mirrors and influences the transmission width.³¹

Figure 7(a) shows the approach used to write phase-shifted gratings with an opaque mask (width of $\sim 300 \mu\text{m}$) placed near the center of the beam to block the central portion of the interference pattern during the writing process. This changes the average index at that point, causing a dephasing between the two ends of the grating and hence the creation of a resonant cavity. This is, to our knowledge, the first report of phase-shifted Bragg gratings written in ChG waveguides and lays a foundation for application in future experiments with further refinement of the process. In Fig. 7(b), the transmission spectra (solid curve) of a phase-shifted grating are shown, fabricated as described in a $2.2 \mu\text{m}$ wide ($H=2.7 \mu\text{m}$, $h=1.0 \mu\text{m}$) quasi-single-mode waveguide (TM polarization). The single, narrow ($<100 \text{pm}$) resonance peak in the transmission spectrum can serve either as a narrow-bandpass filter or as a cavity to strongly enhance the fields and hence the nonlinear optical processes. Modeling (dashed-dotted curve) of this structure using the T -matrix method is able to reproduce the spectrum well.

C. Effect of Birefringence and Higher-Order Modes

Figure 8 shows the transmission spectra of a grating written in a rib waveguide (1.3 cm long, $5.2 \mu\text{m}$ wide, $h=1.0 \mu\text{m}$, $H=2.7 \mu\text{m}$) where birefringence has induced spectral splitting of the TE and TM resonances. As mentioned earlier, the wider waveguide used here supports multiple HOMs that manifest as additional transmission dips observed on the short wavelength side of the main resonance.

Bragg gratings are powerful tools to investigate the modal properties and birefringence of the waveguides.^{34,35} The phase-matching equation defines the Bragg wave-

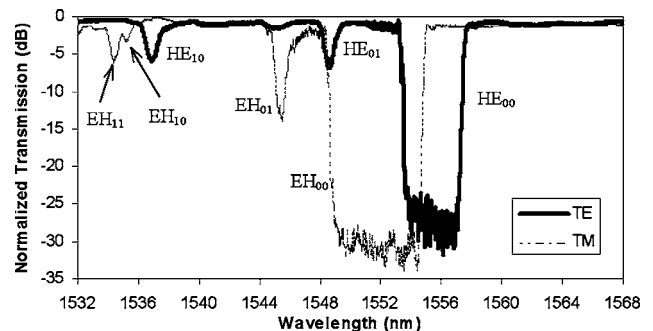


Fig. 8. Spectrum of a grating written in a 1.3 cm long waveguide and rib width of $5.2 \mu\text{m}$ ($h=1.0 \mu\text{m}$, $H=2.7 \mu\text{m}$) for both TE and TM polarizations.

length in terms of the grating period (Λ) and the effective indices (n_{eff}) of the incident (p) and scattered (q) propagating modes:

$$\lambda_{p,q} = \Lambda(n_{\text{eff},p} + n_{\text{eff},q}). \quad (11)$$

For the main resonance, only the fundamental mode is involved, resulting in $p=q=0$. Using the beam propagation method,²⁸ the precise effective modal indices of the fundamental mode for the waveguide in Fig. 8 have been compiled in Table 1 for both TE and TM polarizations. From Table 1, the difference in refractive indices between the EH_{00} and HE_{00} (fundamental TE and TM) modes is $\Delta n_{\text{eff}} \sim 8.45 \times 10^{-4}$, which would give rise to a Bragg wavelength polarization shift of $\Delta\lambda \sim 0.55$ nm. This is much less than the actual ~ 3 nm shift ($\Delta n \sim 5 \times 10^{-3}$) observed in Fig. 8. This would indicate that the waveguide structural birefringence is not the sole cause of this birefringence. Even though photoinduced birefringence of the order of $\Delta n \sim 2 \times 10^{-3}$ has been previously observed in As_2S_3 illuminated by bandgap light ($E \sim 2.3$ eV) (Ref. 36) and a nonuniform refractive index profile in the vertical direction may be expected from the limited absorption length for the 532 nm writing wavelength¹⁶ (~ 3 μm , comparable to our waveguide dimensions), we have observed varied spectral splitting even under identical writing conditions. This suggests other mechanisms, such as stress-induced anisotropy (induced possibly under waveguide fabrication), are present.

Table 1. Comparison between the Bragg Wavelength and Mode Indices Determined from the Spectrum in Fig. 8 and Those Simulated by the Beam Propagation Method

Polarization	Mode	Simulation		
		Experiment Bragg Wavelength (nm)	Effective Index (n_{eff})	Bragg Wavelength (nm)
TM	EH_{00}	1551.5 (λ_0)	2.35981 (n_0)	1551.5
	EH_{01}	1547.0	2.34749	1547.4
	EH_{10}	1536.0	2.31128	1535.5
	EH_{11}	1535.1	2.30217	1532.5
TE	HE_{00}	1555.5 (λ_0)	2.36127 (n_0)	1555.5
	HE_{01}	1549.3	2.34853	1551.3
	HE_{10}	1537.4	2.31768	1541.14

Table 1 also lists the effective indices of the HOMs of the above waveguide. As the input fiber is well aligned to the waveguide and provides good mode overlap with the fundamental mode, we assume that only the fundamental mode ($p=0$) is excited (in agreement with beam propagation modeling). Therefore all the HOM resonances correspond to the fundamental waveguide mode ($p=0$) coupling to a HOM ($q>0$) via the Bragg grating. If λ_0 and λ_q are resonance wavelengths for the fundamental and q th HOMs, respectively, the following relation can be obtained from Eq. (11):

$$\frac{\lambda_q}{\lambda_0} = \frac{n_{\text{eff},q} + n_{\text{eff},0}}{2n_{\text{eff},0}}. \quad (12)$$

Table 1 shows the comparison between the experimental and theoretical resonance wavelengths and shows good agreement. A similar analysis conducted for the HOM observed in Fig. 4 results in a difference of less than 0.7 nm.

The depth of the transmission dips in Fig. 8 depends on the mode-coupling coefficient, which is proportional to the overlap integral between the incident and scattered mode fields and the transverse spatial distribution of the grating refractive index perturbation.³⁴ Figure 9 shows the mode intensity profiles associated with the indices referred to in Table 1. We note that the HOMs do not possess the same symmetry as the incident fundamental mode. Loss of up-down symmetry is expected due to the nonuniform refractive index change distribution; however, the loss of left-right symmetry suggests that the waveguide or grating also exhibits an associated breakdown in symmetry. The relatively low transmission rejection of these respective resonances (compared with the fundamental resonance) suggests that this is a weak effect.

D. Effect of Aging

Another phenomenon we observed was a shift in the Bragg wavelength toward longer wavelengths associated with aging. Figure 10 shows the transmission spectrum of a grating (TE polarization) written in a 1.3 cm long waveguide, as a function of elapsed time after writing. The grating was exposed for 60 s at 6.8 mW. As seen, the grating spectrum shifted ~ 2 nm after a month of storage in a dark, temperature-stabilized location. This shift appears to be produced by a change in grating period by approximately 1 part in 1000. We believe this to be caused by the relaxation of stress induced in the As_2S_3 during the writ-

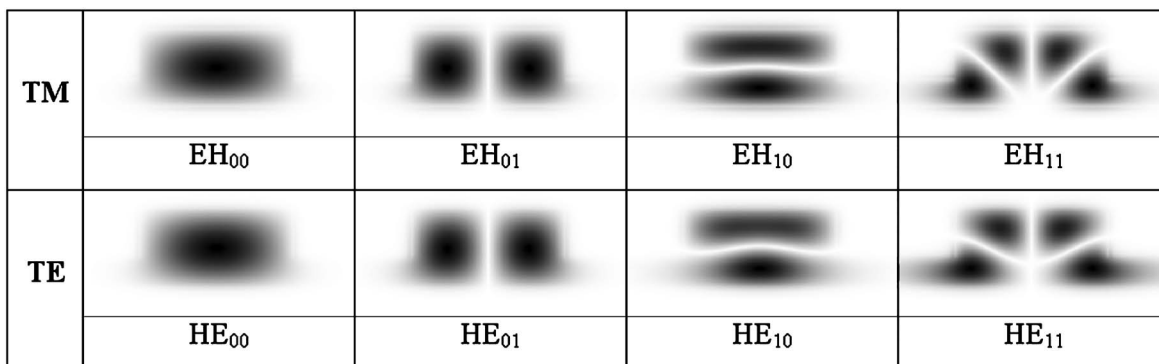


Fig. 9. Mode profiles obtained using the beam propagation method for the modes referred to in Table 1.

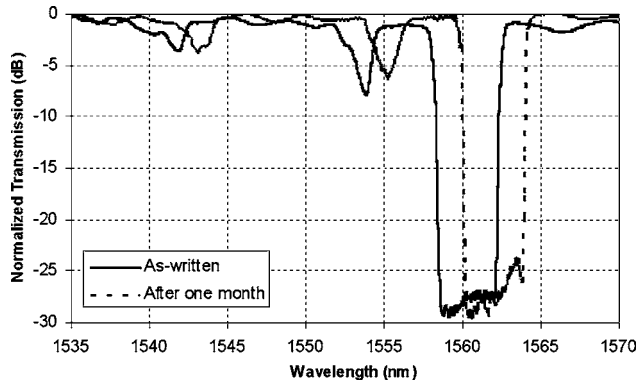


Fig. 10. Transmission spectrum of a grating (TE polarization) written in a 1.3 cm long waveguide measured as written and after one month.

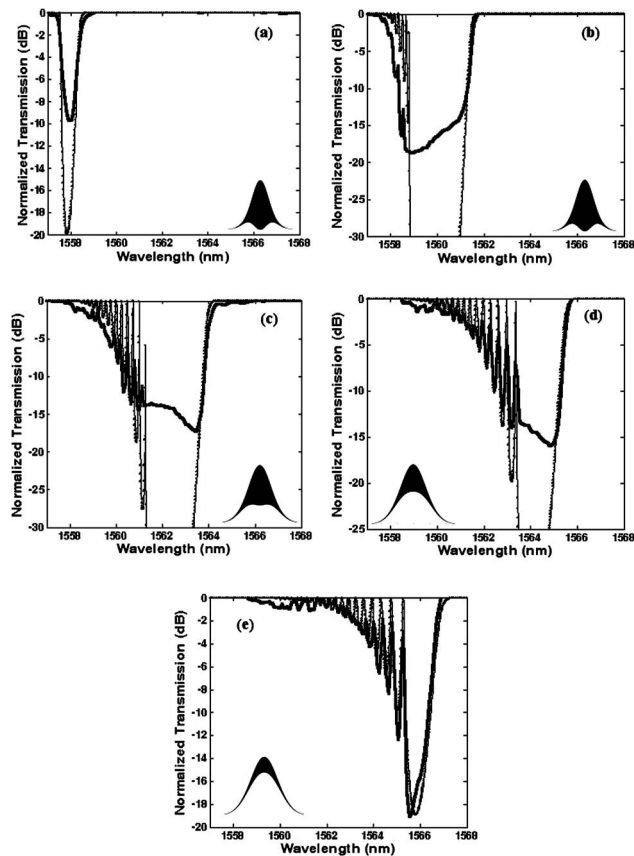


Fig. 11. Evolution of the transmission spectra of a grating during the writing process measured by an *in situ* monitoring setup after (a) 86, (b) 196, (c) 350, (d) 502, (e) 712 s. The thick solid curves represent the experiment, while the points are from modeling. Inset shows the modeled grating refractive profile.

ing process (photoexpansion relaxation) in addition to the stress induced during the waveguide fabrication process (particularly in unannealed As_2S_3 layers).³⁷

E. Grating Growth Dynamics

We used an *in situ* monitoring setup for investigating the growth behavior of the gratings. The setup consisted of two 3-axis translation stages used to couple light from an erbium-doped fiber amplifier ASE source to the waveguide through a polarization control stage, and from the

waveguide to an OSA, via high-NA fibers. Note that previous reports of *in situ* monitoring during growth were based on a Mach-Zehnder writing setup.^{16,24} Our results were obtained while writing a grating in a 5 cm long, 5 μm wide ($H=2.37 \mu\text{m}$, $h=1.25 \mu\text{m}$) waveguide with a total writing power at the waveguide surface of 5.6 mW. TE-polarized light was launched into the waveguide and the sampling interval for recording the transmission spectral data from the OSA was 9 s.

Figures 11(a)–11(e) shows the experimental evolution of the transmission spectra of the grating during writing after 86, 196, 350, 502, and 712 s. Three effects are observed in Fig. 11: (1) the shift of the Bragg wavelength to longer wavelengths; (2) the variation of the 3 dB spectral bandwidth of the grating; and (3) the evolution of the spectral shape and appearance of sidelobes on the short wavelength side of the spectra, implying a significant evolution of the raised Gaussian apodization function.

These effects can be understood by studying the temporal variation of the dc and ac refractive index change as inferred from the Bragg wavelength and the grating bandwidth using the following relations:

$$\Delta n_{\text{dc}}(t) = n_0[\Delta\lambda_B(t)/\lambda_i], \quad (13)$$

$$\Delta n_{\text{ac}}(t) = n_0[\Delta\lambda(t)/\lambda_B(t)]. \quad (14)$$

Here n_0 is the linear refractive index of the grating medium, λ_i is the Bragg wavelength at the initial stage of grating growth (here $\sim 1558 \text{ nm}$), $\Delta\lambda_B(t) = \lambda_B(t) - \lambda_i$, and $\Delta\lambda(t)$ is the 3 dB bandwidth of the grating spectrum at time t . Figure 12 shows the dc and ac refractive index changes versus writing time. As can be seen, Δn_{dc} increases monotonically, tending toward a saturation value of ~ 0.015 for longer exposure times ($t > 580 \text{ s}$). During the grating growth, Δn_{ac} increases to a maximum value (~ 0.0072 at 320 s) and then decreases for longer exposure times. This indicates a decrease in the visibility of interference fringes creating the index modulation since the average index continues to grow. This effect can be understood by observing that, as the refractive index in the regions corresponding to the maxima of the intensity interference pattern begins to increase and then saturates, the refractive index at the troughs between the peaks rises continuously, resulting in a decrease in the Δn_{ac} . The insets in Figs. 11(a)–11(e) are the corresponding grating profiles calculated from Eq. (9) and the inferred index

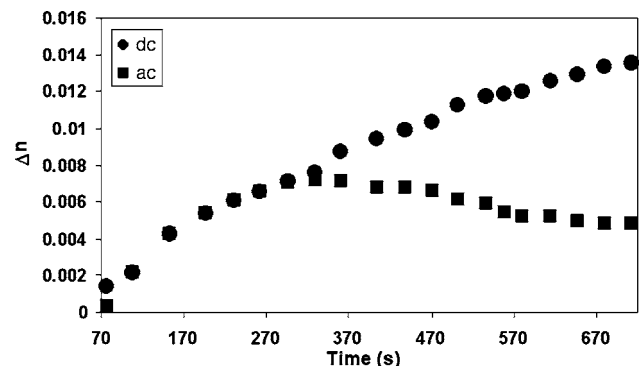


Fig. 12. Behavior of dc and ac refractive index changes over time calculated based on the experimental spectral data.

changes. These profiles clearly show that the ideal apodization function is not retained for long exposure times, causing the average refractive index to vary strongly across the grating and generating sidelobes on the short wavelength side of the main resonance. In fact we can use the inferred values of the dc and ac refractive index in the T -matrix model, and indeed we find that the experimental and modeled spectra are in excellent agreement.

6. CONCLUSION

We report the first high-performance Bragg gratings written in As_2S_3 -based rib waveguides paving the way for a multitude of uses in integrated nonlinear waveguide devices. To generate these gratings, we used a modified Sagnac interferometer, which produced an interference pattern stable over many minutes, as well as the high material photosensitivity of As_2S_3 to achieve strong Bragg gratings, which could be well apodized and phase shifted. In addition, we achieved good agreement with experiment by theoretically modeling the gratings with a 2×2 transfer-matrix formulation. The gratings provided an excellent tool to examine the photonic structure of the waveguides including higher-order modes, birefringence (waveguide-based and photoinduced), and postexposure structural relaxation. We find that birefringence in the waveguides is mainly due to the waveguide geometry and material stress, rather than photoinduced. In addition, structural relaxation is the main process that shifts the grating spectra toward longer wavelengths after grating writing. Finally, *in situ* monitoring allowed us to investigate grating growth during writing. The results verified our understanding of the writing process and pointed toward potential improvements in the writing setup. It further allowed us to determine the optimal point to terminate exposure before saturation effects begin to decrease the visibility of the index modulation.

ACKNOWLEDGMENTS

This work was produced with the assistance of the Australian Research Council (ARC). The Centre for Ultrahigh-bandwidth Devices for Optical Systems is an ARC Centre of Excellence. M. Shokooh-Saremi appreciates the partial support of the Iranian Ministry of Science, Research and Technology.

REFERENCES

- M. Asobe, "Nonlinear optical properties of chalcogenide glass fibers and their application to all-optical switching," *Opt. Laser Technol.* **3**, 142–148 (1997).
- R. E. Slusher, G. Lenz, J. Hodelin, J. Sanghera, L. B. Shaw, and I. D. Aggarwal, "Large Raman gain and nonlinear phase shifts in high-purity As_2S_3 chalcogenide fibers," *J. Opt. Soc. Am. B* **21**, 1146–1155 (2004).
- A. Salimnia, A. Villeneuve, T. V. Galstyan, S. LaRochelle, and K. Richardson, "First- and second-order Bragg gratings in single-mode planar waveguides of chalcogenide glasses," *J. Lightwave Technol.* **17**, 837–842 (1999).
- P. V. Mamyshev, "All-optical data regeneration based on self-phase modulation effect," presented at the 24th European Conference on Optical Communication (ECOC), Madrid, Spain, 20–24 September 1998.
- V. G. Ta'eed, M. Shokooh-Saremi, L. Fu, D. J. Moss, M. Rochette, I. C. M. Littler, B. J. Eggleton, Y. Ruan, and B. Luther-Davies, "Integrated all-optical pulse regenerator in chalcogenide waveguides," *Opt. Lett.* **30**, 2900–2902 (2005).
- L. Fu, M. Rochette, V. Ta'eed, D. Moss, and B. J. Eggleton, "Investigation of self-phase modulation based optical regenerator in single mode As_2S_3 chalcogenide glass fiber," *Opt. Express* **13**, 7637–7644 (2005).
- C. R. Giles, "Lightwave applications of fiber Bragg gratings," *J. Lightwave Technol.* **15**, 1391–1404 (1997).
- B. J. Eggleton, R. E. Slusher, C. M. d. Sterke, P. A. Krug, and J. E. Sipe, "Bragg grating solitons," *Phys. Rev. Lett.* **76**, 1627–1630 (1996).
- P. Yeh, *Optical Waves in Layered Media* (Wiley, 1988).
- J. M. Harbold, F. O. Ilday, F. W. Wise, J. S. Sanghera, V. Q. Nguyen, L. B. Shaw, and I. D. Aggarwal, "Highly nonlinear As–S–Se glasses for all-optical switching," *Opt. Lett.* **27**, 119–121 (2002).
- Y. L. Ruan, W. T. Li, R. Jarvis, N. Madsen, A. Rode, and B. Luther-Davies, "Fabrication and characterization of low loss rib chalcogenide waveguides made by dry etching," *Opt. Express* **12**, 5140–5145 (2004).
- A. Zakery and S. R. Elliott, "Optical properties and applications of chalcogenide glasses: a review," *J. Non-Cryst. Solids* **330**, 1–12 (2003).
- K. Petkov and P. J. S. Ewen, "Photoinduced changes in the linear and non-linear optical properties of chalcogenide glasses," *J. Non-Cryst. Solids* **249**, 150–159 (1999).
- J. M. Laniel, N. Ho, R. Vallee, and A. Villeneuve, "Nonlinear refractive index measurement in As_2S_3 channel waveguides by asymmetric self-phase modulation," *J. Opt. Soc. Am. B* **22**, 437–445 (2005).
- A. Salimnia, K. L. Foulgoc, A. Villeneuve, and T. Galstian, "Photoinduced Bragg reflectors in As–S–Se/As–S based chalcogenide glass multilayer channel waveguides," *Fiber Integr. Opt.* **20**, 151–158 (2001).
- M. Asobe, T. Ohara, I. Yokohama, and T. Kaino, "Fabrication of Bragg grating in chalcogenide glass fibre using the transverse holographic method," *Electron. Lett.* **32**, 1611–1613 (1996).
- S. I. Najafi, *Introduction to Glass Integrated Optics* (Artech House, 1992).
- R. G. Walker, "Simple and accurate loss measurement technique for semiconductor optical waveguides," *Electron. Lett.* **21**, 581–583 (1985).
- R. G. Hunsperger, *Integrated Optics: Theory and Technology*, 5th ed. (Springer-Verlag, 2002).
- R. A. Soref, J. Schmidtchen, and K. Petermann, "Large single-mode rib waveguides in GeSi-Si and Si-on-SiO_2 ," *IEEE J. Quantum Electron.* **27**, 1971–1974 (1991).
- M. Shokooh-Saremi, V. G. Ta'eed, I. C. M. Littler, D. J. Moss, B. J. Eggleton, Y. Ruan, and B. Luther-Davies, "Ultra-strong, well-apodized Bragg gratings in chalcogenide rib waveguides," *Electron. Lett.* **41**, 738–739 (2005).
- N. Ponnampalam, R. G. DeCorby, H. T. Nguyen, P. K. Dwivedi, C. J. Haugen, J. N. McMullin, and S. O. Kasap, "Small core rib waveguides with embedded gratings in As_2S_3 glass," *Opt. Express* **12**, 6270–6277 (2004).
- T. G. Robinson, R. G. DeCorby, J. N. McMullin, C. J. Haugen, S. O. Kasap, and D. Tonchev, "Strong Bragg gratings photoinduced by 633-nm illumination in evaporated As_2S_3 thin films," *Opt. Lett.* **28**, 459–461 (2003).
- R. Vallee, S. Frederick, K. Asatryan, M. Fischer, and T. Galstian, "Real-time observation of Bragg grating formation in As_2S_3 chalcogenide ridge waveguides," *Opt. Commun.* **230**, 301–307 (2004).
- H.-G. Frohlich and R. Kashyap, "Two methods of apodization of fibre Bragg gratings," *Opt. Commun.* **157**, 273–281 (1998).

26. T. Erdogan, "Fiber grating spectra," *J. Lightwave Technol.* **15**, 1277–1294 (1997).
27. B. -G. Kim and E. Garmire, "Comparison between the matrix method and the coupled-wave method in the analysis of Bragg reflector structures," *J. Opt. Soc. Am. A* **9**, 132–136 (1992).
28. M. D. Feit and J. A. Fleck, "Computation of mode properties in optical fiber wave-guides by a propagating beam method," *Appl. Opt.* **19**, 1154–1164 (1980).
29. A. Melloni, M. Chinello, and M. Martinelli, "All-optical switching in phase-shifted fiber Bragg grating," *IEEE Photon. Technol. Lett.* **21**, 42–44 (2000).
30. R. Kashyap, P. F. McKee, and D. Armes, "UV written reflection grating structures in photosensitive optical fibres using phase-shifted phase masks," *Electron. Lett.* **30**, 1977–1978 (1994).
31. J. Canning and M. G. Sceats, "Pi-phase-shifted periodic distributed structures in optical fibres by UV post processing," *Electron. Lett.* **30**, 1344–1345 (1994).
32. D. Uttamchandani and A. Othonos, "Phase-shifted Bragg gratings formed in optical fibres by postfabrication thermal processing," *Opt. Commun.* **127**, 200–204 (1996).
33. A. K. Ahuja, P. E. Steinvurzel, B. J. Eggleton, and J. A. Rogers, "Tunable single phase-shifted and superstructure gratings using microfabricated on-fiber thin film heaters," *Opt. Commun.* **184**, 119–125 (2000).
34. V. Ta'eed, D. Moss, B. J. Eggleton, D. Freeman, S. Madden, M. Samoc, B. Luther-Davies, S. Janz, and D. Xu, "Higher order mode conversion via focused ion beam milled Bragg gratings in silicon-on-insulator waveguides," *Opt. Express* **12**, 5274–5284 (2004).
35. C. V. Poulsen, J. Hubner, T. Rasmussen, L.-U. A. Andersen, and M. Kristensen, "Characterization of dispersion properties in planar waveguides using UV-induced Bragg gratings," *Electron. Lett.* **31**, 1437–1438 (1995).
36. K. Tanaka, K. Ishida, and N. Yoshida, "Mechanism of photoinduced anisotropy in chalcogenide glasses," *Phys. Rev. B* **54**, 9190–9195 (1996).
37. O. Nordman, N. Nordman, and A. Ozols, "Influence of the age of amorphous nonannealed As₂S₃ thin films on holographic properties," *Opt. Commun.* **145**, 38–42 (1998).